Materials Research Express

PAPER

Zero-Field ODMR and relaxation of Si-vacancy centers in 6*H*-SiC

Harpreet Singh[1] [ID] , Andrey N Anisimov[1] [ID], Pavel G Baranov[2] [ID] and Dieter Suter[1] [ID]

[1] Fakultät Physik, Technische Universität Dortmund, D-44221 Dortmund, Germany
[2] Ioffe Institute, St. Petersburg 194021, Russia

E-mail: harpreet.singh@tu-dortmund.de

Abstract

Silicon vacancies in silicon carbide (SiC) have been proposed as interesting candidates for quantum technology applications such as quantum sensing and quantum repeaters. SiC exists in many polytypes with different plane stacking sequences, and in each polytype, the vacancies can occupy a variety of different lattice sites. In this work, we focus on the three important charged silicon vacancies in the 6*H*-SiC polytype. We record the photoluminescence and continuous-wave optically detected magnetic resonance (ODMR) spectra at different radio-frequency power levels and different temperatures. We individually select the zero-phonon lines of the different silicon vacancies at low temperatures and record the corresponding ODMR spectra. ODMR allows us to correlate optical and magnetic resonance spectra and thereby separate signals from V_1 and V_3. The results also explain the observed sign change of the ODMR signal as a function of temperature.

1. Introduction

Silicon carbide (SiC) is an interesting material for a range of applications that rely on its wide bandgap and established manufacturing processes [1–8]. It contains different types of silicon vacancies [9–13] and silicon-carbon divacancies [14–16], which show remarkable spin properties that make them promising candidates for new quantum technologies [17, 18]. As a specific example, negatively charged silicon vacancies (V_{Si}^-), have spin 3/2 [19]. Irradiation with visible or near-infrared light results in non-thermal population of the spin states. Two characteristic parameters of V_{Si}^- centers are the emission wavelength and the zero field splitting (ZFS).

In the low temperature photoluminescence (PL) spectra, different centers can be identified by their emission wavelengths. In sequence of increasing wavelengths, they are therefore labeled V_1, V_2 and V_3 in the case of the 6*H*-SiC polytype [20]. In terms of the local structure, they are associated with different lattice sites where the environment has cubic (*k*) or hexagonal (*h*) symmetry. The correspondence between emission wavelength and lattice sites is a matter of ongoing controversy in 6*H*-SiC [9, 14, 21–23].

In a previous paper, silicon vacancies in 6*H*-SiC were characterised [24] in terms of their photoluminescence as well as their spin Hamiltonian, using ODMR. Since ODMR correlates optical properties with energy differences between spin states, it provides a useful approach for associating the zero-field splittings with the emission wavelengths. The goal of this work is to identify the different types of V_{Si}^- centers in 6*H*-SiC. For this purpose, we combine photoluminescence (PL) measurements at different wavelengths with radio-frequency excitation of the spin transitions to record ODMR spectra under a range of different conditions, including its temperature dependence. In previous work [25], we measured the relaxation of silicon vacancies in 6*H*-SiC with almost inverted spin isotope concentrations, i.e., ^{13}C (4.7%) and ^{29}Si (0.1%), whereas the 6*H*-SiC sample used in this study has natural abundance of ^{13}C (1.1%) and ^{29}Si (4.7%). In this work, we measure the relaxation rates of the vacancies and compare them with the results obtained in a different sample [25].

This work is structured as follows: section 2 introduces the spin system of the sample, as well as its photoluminescence as a function of the direction of the emission with respect to *c*-axis, and separates it into the contributions of the 3 types of vacancies. Section 3 shows the temperature-dependent ODMR spectra for emission parallel and perpendicular to the *c*-axis. To distinguish the contributions from the different types of

centers, we record signals at different wavelengths separately. Section 4 contains the spin-lattice and spin-spin relaxation times obtained by time-resolved ODMR. Section 5 contains a brief discussion and concluding remarks.

2. System

For creating silicon vacancies homogeneously, the sample can be irradiated with neutrons or electrons [26]. Neutron irradiation leads to more lattice damage than electron irradiation and creates many other unwanted defects, resulting in faster relaxation rates of the vacancy spins [27]. For this work, to create V_{Si}^- centers, the 6*H*-SiC crystal was irradiated with electrons with a dose of 10^{18} cm^{-2} and an energy of 2 MeV at room temperature [28]. More details of the sample preparation are given in appendix A.

At the silicon vacancy site, four dangling sp^3 orbitals contribute four electrons. In addition, the silicon vacancy can capture one or two electrons, depending on the Fermi level, and become a negatively charged silicon vacancy (V_{Si}^-). Here, we only consider centers with a single negative charge, which have a spin of 3/2 [19]. The energy levels of these vacancies can be determined from a PL spectrum.

2.1. Photoluminescence
We start the characterisation of the sample with the photoluminescence spectra. Depending on the transition dipole, whose orientation varies with the different types of vacancies [24, 29], the PL emission shows an orientation dependence. We therefore recorded PL spectra for emission parallel and perpendicular to the *c*-axis. The detailed description of the PL setup is given in appendix B.

Figures 1(a) and (b) show the PL spectra recorded for emission perpendicular and parallel to the *c*-axis at 5 K. In addition to the full spectra, where we used an 850 nm long-pass (LP) filter to suppress scattered laser light, we also recorded spectra with 860 nm, 890 nm and 905 nm bandpass (BP) filters. The zero phonon lines (ZPL) of the different V_{Si}^- are clearly visible in the spectra at 865 nm (V_1), 887 nm (V_2), and 908 nm (V_3) [9, 21]. Comparison of the two sets of spectra shows that V_1 and V_3 emit more PL parallel to the *c*-axis, while V_2 emits more perpendicular to the *c*-axis [24, 25, 30].

The assignment of the emission lines to specific lattice sites was debated in the literature. An early study of 6*H*-SiC [9], indicated that V_1 and V_3 correspond to V_{Si}^- at the cubic lattice sites k_1 and k_2 and V_2 corresponds to the hexagonal lattice site *h*. However, more detailed studies indicate that V_1 corresponds to the hexagonal lattice site *h* and V_2 and V_3 to the cubic lattice sites k_2 and k_1 respectively [14, 23]. We adopt the latter assignment here.
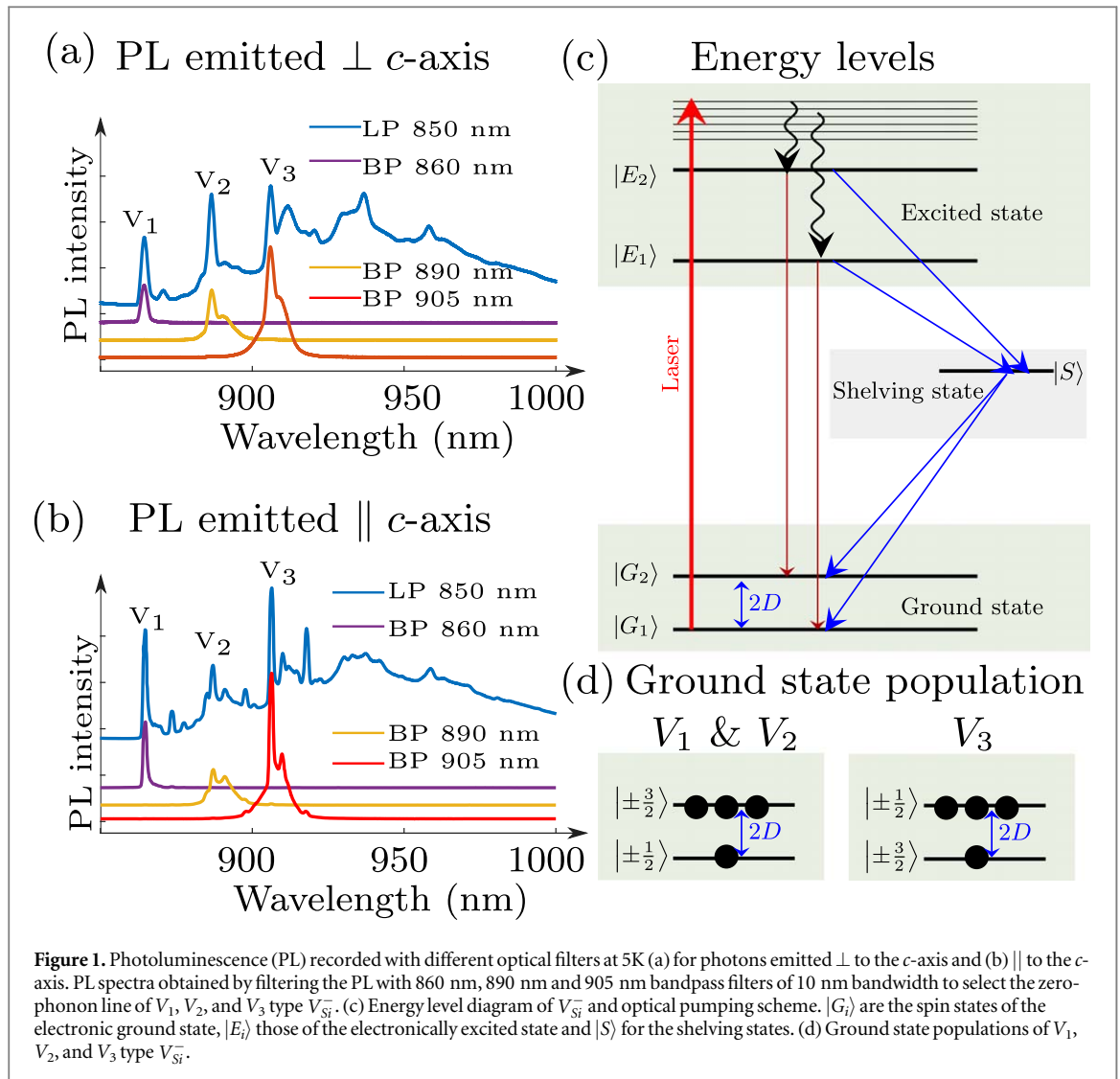
2.2. Spin
We consider the $S = 3/2$ spin of a of V_{Si}^- center in the absence of an external magnetic field. Figure 1(c) shows the relevant part of the energy level diagram. The states $|G_1\rangle$ and $|G_2\rangle$ are doubly degenerate spin substates of the electronic ground state with $m_s = \pm 1/2$ and $\pm 3/2$ in the case of V_1 and V_2 [14, 21]. In the case of V_3, the ZFS is negative and the lowest energy states are therefore $m_s = \pm 3/2$ [14]. Similarly, the states $|E_1\rangle$ and $|E_2\rangle$ are spin states of the electronically excited state. The state $|S\rangle$ represents the shelving state (for simplicity, we consider $|S\rangle$ as a single level, although it appears that multiple states might participate in the role of the shelving state.), which has spin $S = 1/2$ and plays an essential role for generating spin polarization by optical pumping [21, 31]. Laser illumination excites transitions from the ground states $|G_1\rangle$ and $|G_2\rangle$ to the excited states $|E_1\rangle$ and $|E_2\rangle$. From the excited states $|E_i\rangle$, most of the population falls back to the ground states $|G_i\rangle$ due to spontaneous emission. A smaller fraction undergoes intersystem crossing (ISC) to the shelving state $|S\rangle$, and from there, preferentially populates the ground state $|G_2\rangle$, as shown in figure 1, where $|G_2\rangle$ represent spin sublevels $|\pm 3/2\rangle$ in case of V_1 and V_2 and $|\pm 1/2\rangle$ in the case of V_3 [14].

In the absence of an external magnetic field, the effective spin Hamiltonian is

$$\mathcal{H} = D(S_z^2 - 5/4), \tag{1}$$

where D is the zero-field splitting constant whose value depends on the environment of the center. S_z is the electron spin operator along the *z* axis (|| crystal *c* axis). In the magnetic resonance spectra, we therefore expect a single resonance line at frequency $2D$ for every type of vacancy. The 1D projections in figure 2(a) and (b) show, as examples, ODMR spectra of a 6*H*-SiC sample containing three different types of vacancies, recorded parallel and perpendicular to the *c*-axis, respectively, using the 850 nm LP filter. They consist of two resonance lines close to 28 MHz and 130 MHz. The assignment of these resonance lines to the different types of V_{Si}^- in 6*H*-SiC has been somewhat contentious, in particular with respect to V_1. Table 1 provides a summary of the relevant parameters. While Davidsson *et al* [14] assume that V_1 contributes to the resonance near 28 MHz, Biktagirov *et al* [23] suggest that it is close to zero and therefore not observable. In the following section, we resolve this issue by measuring ODMR spectra at low temperatures and separating the PL from the ZPLs of the 3 different vacancies using suitable optical bandpass filters.

Figure 1. Photoluminescence (PL) recorded with different optical filters at 5K (a) for photons emitted ⊥ to the *c*-axis and (b) ∥ to the *c*-axis. PL spectra obtained by filtering the PL with 860 nm, 890 nm and 905 nm bandpass filters of 10 nm bandwidth to select the zero-phonon line of V_1, V_2, and V_3 type V_{Si}^{-}. (c) Energy level diagram of V_{Si}^{-} and optical pumping scheme. $|G_i\rangle$ are the spin states of the electronic ground state, $|E_i\rangle$ those of the electronically excited state and $|S\rangle$ for the shelving states. (d) Ground state populations of V_1, V_2, and V_3 type V_{Si}^{-}.

3. Optically detected magnetic resonance

ODMR combines optical measurements with electron spin resonance (ESR) spectroscopy. Compared to conventional ESR, this double resonance technique increases the sensitivity and information content of magnetic resonance [32–34]. For low-temperature ODMR, we placed the sample in a liquid helium flow cryostat and irradiated it with 785 nm laser light. The emitted PL was collected using a convex lens and focused with another convex lens on an avalanche photodiode (APD) via a suitable optical filter. The photocurrent was measured with a lock-in amplifier. A radio-frequency (RF) field was applied to the sample through a wire (for continuous-wave ODMR) or a coil (for pulsed experiments), terminated with a 50-Ohm resistor. To reduce background signal, we modulated the RF with a TTL signal from a digital word generator (DWG) and demodulated the APD signal with a lock-in amplifier referenced to the TTL signal. Appendix C provides a detailed description of the ODMR setup and the ODMR dependence on RF power.

3.1. Temperature dependence

Figures 2(a) and (b) show the ODMR spectra for the range of temperatures from 5 K to 290 K when the PL is recorded parallel and perpendicular to the *c*-axis using an RF power of 26 dBm (0.4 W). The horizontal axis corresponds to the RF frequency, and the vertical axis to the temperature. The color represents the relative change of PL, as indicated by the scale bar on the right. The ODMR signal near 130 MHz, which corresponds to V_2, increases with decreasing temperature while the ODMR signal near 28 MHz, which is due to V_1/V_3, decreases. We recorded larger ODMR signals (ΔPL/PL) when the PL is emitted parallel to the *c*-axis in the case of V_1/V_3, whereas the ODMR signal of V_2 was larger for emission ⊥*c*. In both orientations, the V_2 signal increases with decreasing temperature, while it gets smaller in the case of V_1/V_3. However, for PL emitted
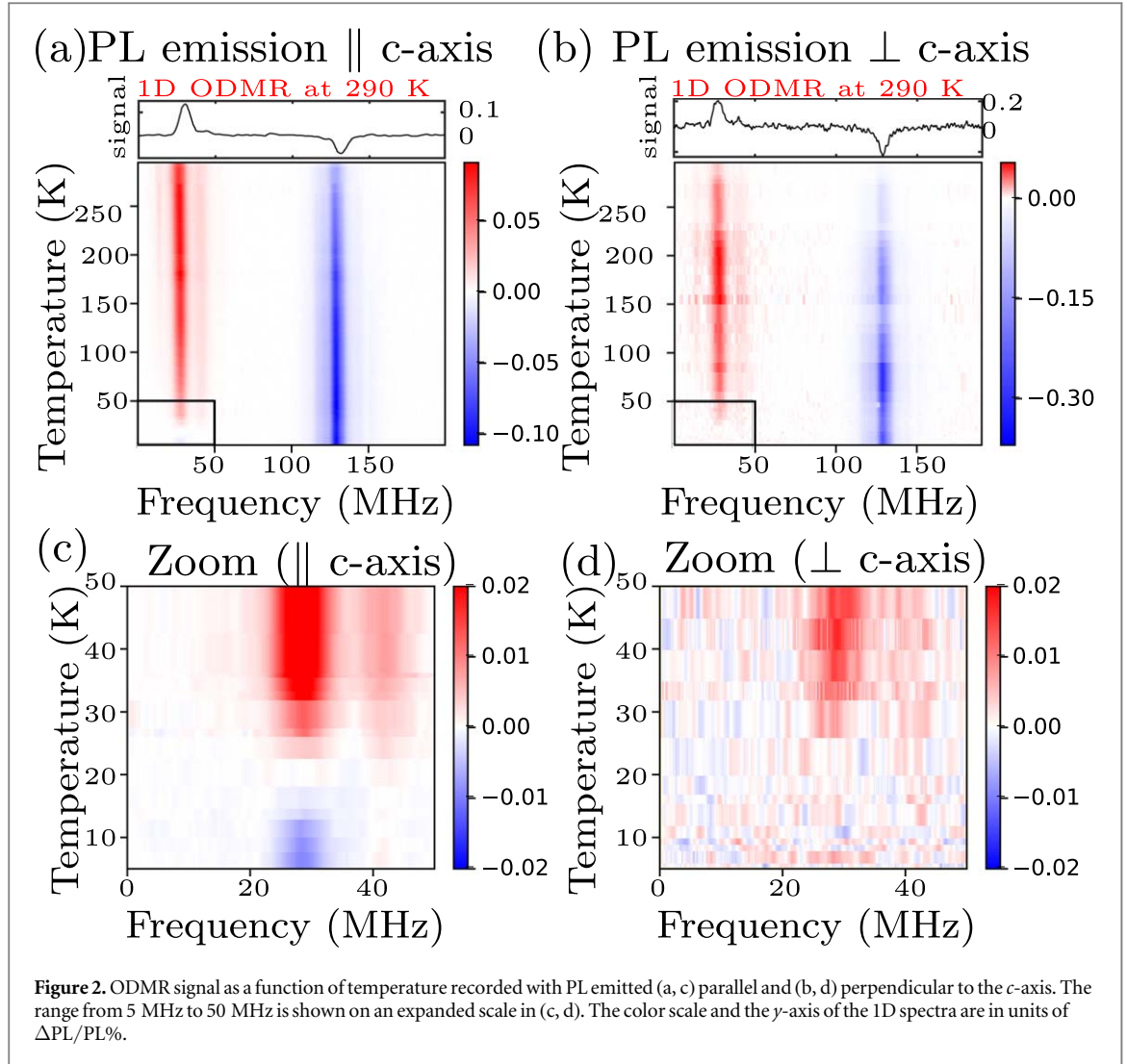
Figure 2. ODMR signal as a function of temperature recorded with PL emitted (a, c) parallel and (b, d) perpendicular to the *c*-axis. The range from 5 MHz to 50 MHz is shown on an expanded scale in (c, d). The color scale and the *y*-axis of the 1D spectra are in units of ΔPL/PL%.

Table 1. Experimental values for the zero field splittings (ZFS) 2*D* for the 3 types of V_{Si}^{-} in 6*H*-SiC. The upper indices *g* refer to the electronic ground states. The values and the proposed assignments to the different types of centers are taken from 3 earlier publications.

Center	Sorman *et al* [9]	Biktagirov *et al* [23]	Davidsson *et al* [14]
Exp	Exp	Exp	Exp
$2D^g$ (Site)	$2D^g$ (Site)	$\lvert 2D^g \rvert$ (Site)	$\lvert 2D^g \rvert$ (Site)
V_1	27.6 MHz (k_1)	0 (*h*)	26.6 MHz (*h*)
V_2	128.4 MHz (*h*)	128 MHz (k_2)	128 MHz (k_2)
V_3	27.6 MHz (k_2)	28 MHz (k_1)	27.8 MHz (k_1)

parallel to the *c*-axis, the ODMR signal near 28 MHz changes sign. Figure 2 (c), shows that the ODMR signal vanishes at 22 K and becomes negative at 15 K. At even lower temperatures, the negative signal increases in magnitude.

Figure 3(a) and (b) show the measured frequency of the ODMR resonance lines that correspond to the ZFS as a function of temperature. (a) corresponds to the V_2 center while the resonance line near 28 MHz is dominated by the signal from V_3 in the temperature range from 36 K to 295 K. The extracted data are fitted to the function
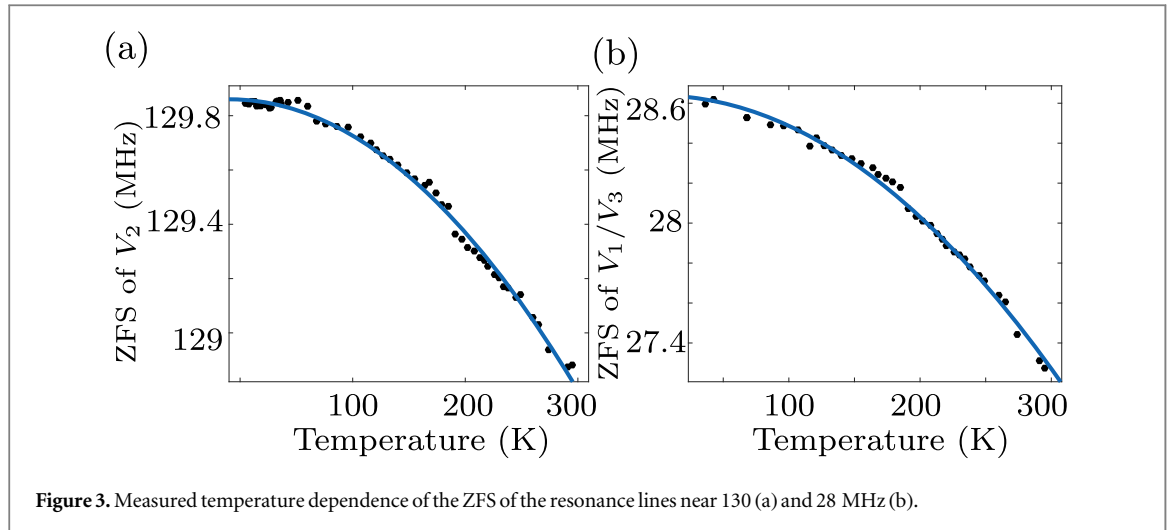
$$ZFS(T) = ZFS_0 + b\,T^2. \tag{2}$$

Figure 3. Measured temperature dependence of the ZFS of the resonance lines near 130 (a) and 28 MHz (b).
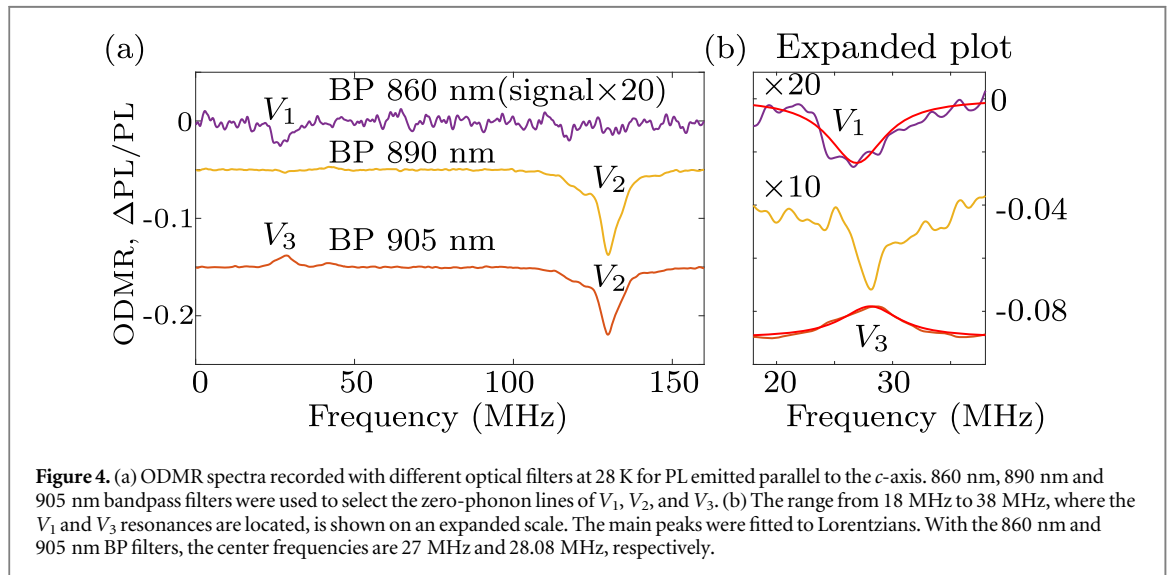

Figure 4. (a) ODMR spectra recorded with different optical filters at 28 K for PL emitted parallel to the *c*-axis. 860 nm, 890 nm and 905 nm bandpass filters were used to select the zero-phonon lines of V_1, V_2, and V_3. (b) The range from 18 MHz to 38 MHz, where the V_1 and V_3 resonances are located, is shown on an expanded scale. The main peaks were fitted to Lorentzians. With the 860 nm and 905 nm BP filters, the center frequencies are 27 MHz and 28.08 MHz, respectively.

The best fits are obtained for the parameters $ZFS_0 = 129.9 \pm 0.5$ MHz and 28.64 ± 0.02 MHz, $b = (-1.19 \pm 0.02) \times 10^{-5}$ MHz K^{-2} and $(-1.52 \pm 0.02) \times 10^{-5}$ MHz K^{-2} for V_2 and V_1/V_3, respectively. These results show a temperature dependence in contrast to earlier reports that suggested the ground-state ZFS does not vary with temperature [35]. The excited-state ZFS of V_{Si}^- in SiC (both for 4H and 6H polytypes) is larger compared to the ground-state ZFS. Temperature dependence studies of the excited-state ZFS have already been reported experimentally [36] and theoretically [37] for 4H-SiC. In the case of nitrogen vacancies (NV) in diamond, temperature-dependent variations in the ground-state ZFS have been attributed to the effect of macroscopic thermal expansion and the resulting changes in microscopic equilibrium positions. This phenomenon accounts for approximately 15 % of the observed decrease in the ground-state ZFS [38]. However, in the case of V_{Si}^- in 6*H*-SiC, the ZFS decreases with temperature by approximately 1% to 5%, depending on the type of vacancy.

3.2. Optically selective detection

For a better identification of the different ODMR signals, we only collect PL from specific wavelength ranges by passing it through different optical filters. Figure 4(a) shows the ODMR spectra recorded with different bandpass (BP) filters at 28 K for PL emitted ∥*c*-axis. The top, middle, and bottom spectra were recorded with 860 nm, 890 nm, and 905 nm BP (10 nm bandwidth) filters, which predominantly select PL from the zero-phonon line (ZPL) of the V_1, V_2, and V_3 vacancies, respectively.

The top spectrum (860 nm BP), contains only a small negative peak near 27 MHz. This differs strongly from the 1D projections in figure 2(a) and the ODMR spectra in figure C2 recorded with the 850 nm LP filter, where we observed two resonances near 28 MHz and 130 MHz. Since the 860 nm BP filter selects the ZPL of V_1, we
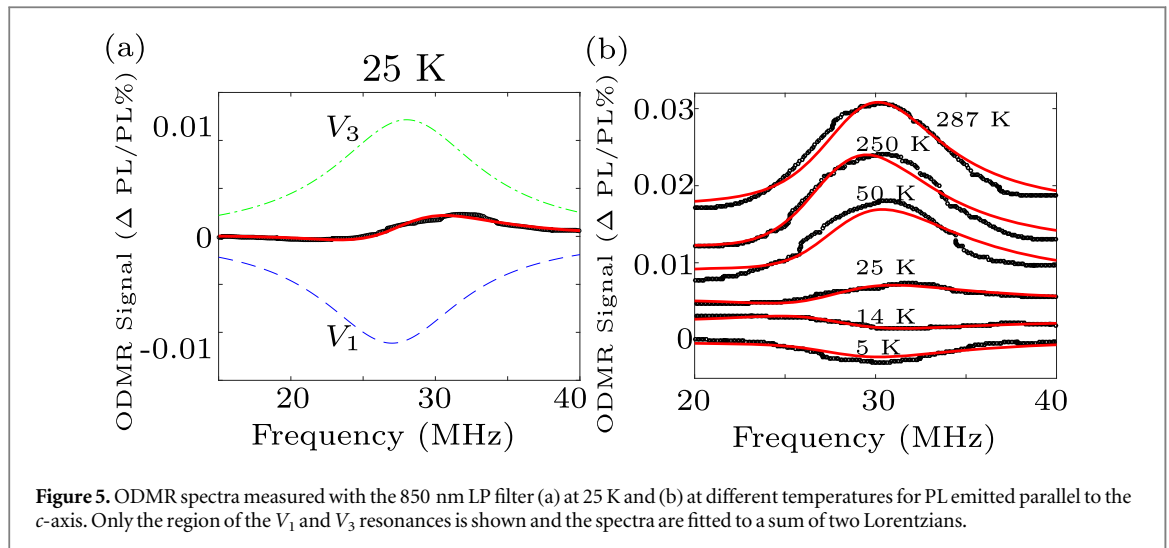
Figure 5. ODMR spectra measured with the 850 nm LP filter (a) at 25 K and (b) at different temperatures for PL emitted parallel to the *c*-axis. Only the region of the V_1 and V_3 resonances is shown and the spectra are fitted to a sum of two Lorentzians.

assign the negative peak at 27 MHz to V_1. Since the signal is quite small under these conditions, we expanded the vertical scale of the top spectrum by a factor of 20 to make the peak visible.

The middle ODMR spectrum was recorded with a BP filter centered at the ZPL of V_2. It is dominated by a signal near 130 MHz, which we therefore attribute to V_2. The bottom ODMR spectrum was recorded with the 905 nm BP filter; we observe one negative and two positive peaks. We attribute the positive peak at 28.1 MHz to the V_3 center, whose ZPL coincides with the center of the 905 nm BP filter. The negative peak at 129.93 MHz is due to the phonon sidebands (PSB) of V_2, which extend well into the range of the 905 BP filter.

Figure 4(b) shows the frequency range from 18 MHz to 38 MHz, where the signals from V_1 and V_3 are centered, on an expanded scale. In the top spectrum, the signal from V_1 dominates, in the bottom spectrum that from V_3.

3.3. Separating the contributions from V_1 and V_3

As discussed in the introduction, there is conflicting evidence on the ZFS of V_1 and V_3. The experiments presented in subsection 3.1 and 3.2 were designed to provide data for distinguishing between them. The results can be interpreted consistently if we assume that the ZFS splittings of V_1 and V_3 are both close to 28 MHz but have slightly different frequencies (27 MHz and 28 MHz) and contribute to the ODMR spectrum with opposite signs: for V_1, the ODMR signal is negative ($\Delta PL/PL < 0$), for V_3 it is positive. Since the combined linewidth is larger than the separation between the two resonance frequencies, only a single line is observed and the two signals partially cancel.
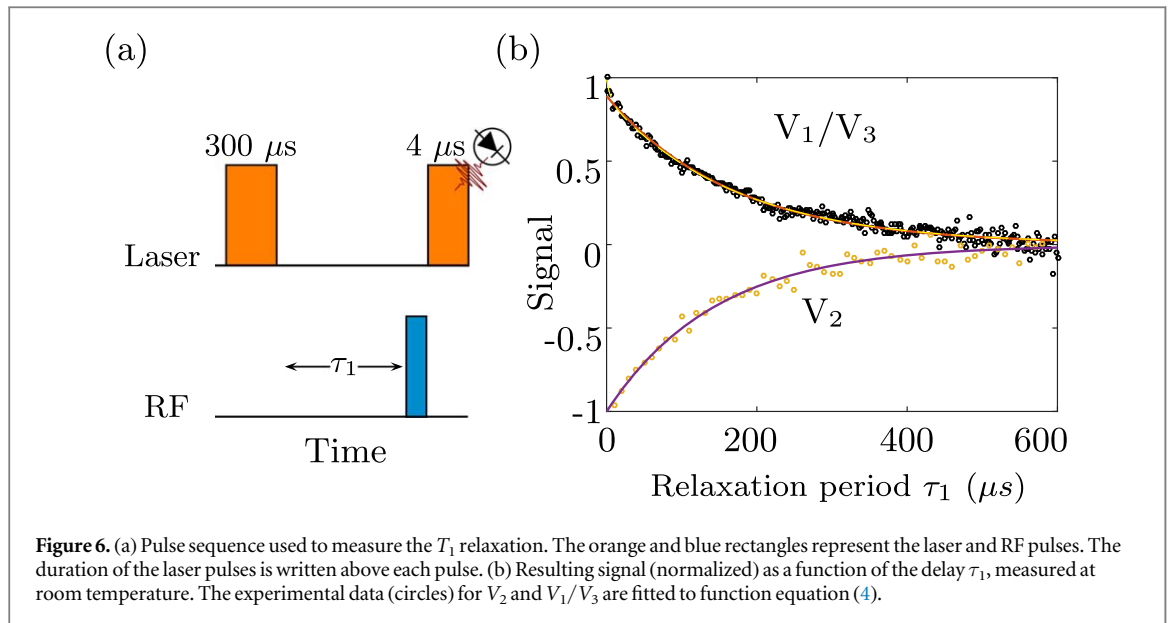
The signals from the two centers also have different temperature dependence. At low temperatures, the V_1 signal at 27 MHz dominates, resulting in an overall negative signal but at high temperatures, the V_3 signal at 28 MHz dominates, resulting in an overall positive signal. For a more detailed analysis, we compare the experimental signal at different temperatures to a theoretical spectrum consisting of two Lorentzians with the frequencies of V_1 and V_3 and opposite amplitudes

$$S(f, T) = \frac{A_1(T)\sigma_1}{(f - ZFS_1)^2 + \sigma_1^2} + \frac{A_3(T)\sigma_3}{(f - ZFS_3)^2 + \sigma_3^2}, \tag{3}$$

using the temperature coefficient $b = (-1.52 \pm 0.02) \times 10^{-5}$ MHz K^{-2} in equation (2) for V_1 and V_3. The values of the ZFS at $T = 0$ were determined from the spectra measured with optical filters at 28 K as $ZFS_0 = 27$ MHz and 28 MHz for V_1 and V_3. The linewidths $\sigma_1 = 5.9$ MHz and $\sigma_3 = 6.1$ MHz were also taken from the spectra measured at 28 K.

Figure 5(a) shows the ODMR spectrum at 28 K fitted to a sum of two Lorentzians at 27 and 28 MHz and opposite amplitudes. Figure 5(b) shows the ODMR spectra for the frequency range 10 to 50 MHz at different temperatures, together with a fitted signal, where only the amplitudes A_i were taken as fitting parameters to measure the contributions from V_1 and V_3. Overall, the superposition of the two resonance lines yields good agreement with the experimental data for temperatures < 50 K, with a slight deviation between the fitted and experimental data above 50 K. This deviation may be due to the change in ZFS with temperature, as shown in figure 3, as well as temperature-induced variations in the crystal's stress [39].

For PL emitted $\perp c$, the signal near 28 MHz decreases with temperature but does not become negative, as shown in figure 2(d). This is also consistent with the assumption that the negative signal is associated with V_1: as

Figure 6. (a) Pulse sequence used to measure the T_1 relaxation. The orange and blue rectangles represent the laser and RF pulses. The duration of the laser pulses is written above each pulse. (b) Resulting signal (normalized) as a function of the delay τ_1, measured at room temperature. The experimental data (circles) for V_2 and V_1/V_3 are fitted to function equation (4).

shown in appendix E, V_1 emits less PL perpendicular to the *c*-axis as shown in figure 1 and therefore can not dominate over the contribution from V_3.

4. Relaxation measurements

In this section we focus on the evolution of the spin system towards thermal equilibrium, which is driven by interactions with the environment [40–42]. Each type of silicon vacancies has a different structure and therefore different interactions with the environment that can be probed by relaxation measurements.

4.1. Population relaxation

The spin-lattice interaction drives the spin system towards thermal equilibrium with its environment. Under our experimental conditions, the thermal equilibrium spin state is completely unpolarised, i.e. the density operator is proportional to the unit operator. The time scale on which the system approaches this equilibrium state is characterized by the spin-lattice relaxation time T_1. Figure 6(a) shows the pulse sequence used to measure the T_1 relaxation time. A 300 μs laser pulse of 785 nm wavelength was applied to polarize the spin system, which was then allowed to evolve for a time τ_1. An RF pulse with flip angle π was applied before measuring the remaining spin polarisation with a second laser pulse of 4 μs. The measured signal was subtracted from the reference signal obtained without applying the RF pulse [25, 28, 31]. Figure 6(b) shows the measured signal versus the delay τ_1. The recorded experimental data can be fitted by an exponential

$$S_\pi(\tau_1) - S_0(\tau_1) = A\,e^{-\tau_1/T_1}, \tag{4}$$

where $S_\pi(\tau_1)$ ($S_0(\tau_1)$) is the optical signal recorded when a π-pulse was applied (not applied) before measuring the remaining spin polarization. At room temperature, the extracted relaxation times T_1 were $145 \pm 2\,\mu$s for V_2 and $166 \pm 2\,\mu$s for V_1/V_3. These measured values are in the same range as those from previous experimental studies on V_2 type vacancies in 4H-SiC with naturally abundant spin isotopes, conducted at room temperature [43, 44]. The T_1 relaxation of the silicon vacancy is influenced by various environmental spins, including spin-1/2, spin-1, and spin-3/2 point defects [45].

4.2. Dephasing

Relaxation affects not only the populations, but also the coherence of the spins [46]. While population relaxation is dominated by fluctuations at the Larmor frequency, coherence dephases under the influence of (quasi-) static interactions. A free induction decay (FID) for V_{Si}^- was measured using the Ramsey scheme [47]. The dephasing time constant T_2^* was 42 ± 4 ns for V_2 and 65 ± 5 ns for V_1/V_3 [28]. Details of the pulse sequence used and experimental data obtained are given in appendix D.

Next, we focus on homogeneous dephasing, which can be measured using the spin-echo experiment [48]. We refer to the time constant of the spin-echo decay as T_2. Figure 7(a) shows the pulse sequence. The system was again polarised with a 300 μs laser pulse. The first RF pulse with flip-angle $\pi/2$ generated coherence between the
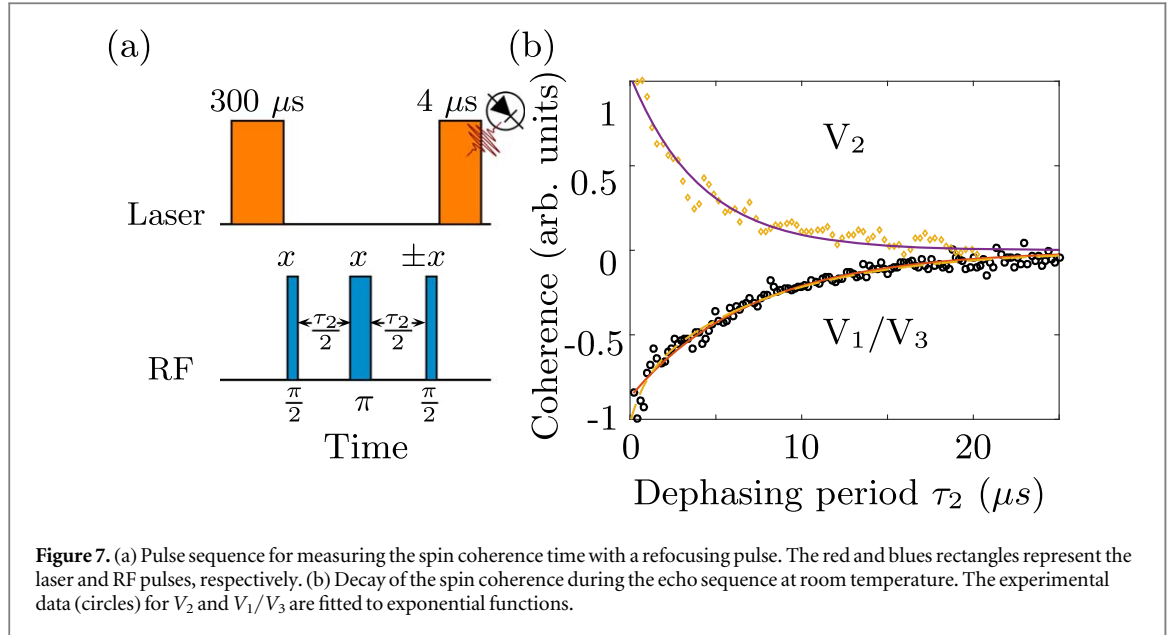
Figure 7. (a) Pulse sequence for measuring the spin coherence time with a refocusing pulse. The red and blues rectangles represent the laser and RF pulses, respectively. (b) Decay of the spin coherence during the echo sequence at room temperature. The experimental data (circles) for V_2 and V_1/V_3 are fitted to exponential functions.

Table 2. Comparison of room-temperature relaxation times of two 6H-SiC samples.

Exp	$^{13}C\,(1.1\,\%)\,\&\,^{29}Si\,(4.7\,\%)$		$^{13}C\,(4.7\,\%)\,\&\,^{29}Si\,(0.1\,\%)$ [25]	
	V_1/V_3	V_2	V_1/V_3	V_2
T_1	166 μs	142 μs	142 μs	107 μs
T_2^*	65 ns	42 ns	38 ns	31 ns
$T_2^{spin-echo}$	7.1 μs	4.6 μs	3.7 μs	3.3 μs
T_2^{CPMG}	57 μs	47 μs	56 μs	51 μs

states $\pm 3/2 \longleftrightarrow \pm 1/2$. The inhomogeneous dephasing was reversed with a π pulse, which generated a spin-echo at time τ_2 after the initial $\pi/2$ pulse. A second $\pi/2$ RF pulse at the time of the echo converted the remaining coherence into population difference, which was measured by the final laser pulse [25, 31]. Figure 7(b) shows the experimental signal versus the delay τ_2 at room temperature. The recorded experimental data can again be fitted to a single exponential and the extracted dephasing times T_2 were 4.1 ± 0.4 μs and 7.1 ± 1.7 μs for V_2 and V_1/V_3, respectively, roughly 2 orders of magnitude longer than T_2^*. The spin-echo data for V_1/V_3 does not fit well to the single exponential, so we also compared it to a sum of 2 exponentials ($A\ e^{-\tau_2/T_2^s} + B\ e^{-\tau_2/T_2^f}$), as shown in figure 7 with a yellow dashed curve ($A = -0.8 \pm 0.1$, $T_2^s = 7.7 \pm 0.3$ μs, $B = -0.2 \pm 0.1$, and $T_2^f = 0.8 \pm 0.4$ μs). The chi-square for the double exponential Fit is 0.33, which is slightly better than what we obtained for the single exponential fit (chi-square for single exponential fit: 0.37). The observed spin echo-time is longer than that measured previously in a similarly prepared 6H-SiC sample with different spin isotopic concentration [25].

Next, we applied multiple refocusing pulses to further extend the coherence lifetime at room temperature. These refocusing pulses remove the dephasing effect of non-static perturbations that have longer correlation times than the spacing between the refocusing pulses. We utilized the Carr-Purcell-Meiboom-Gill (CPMG) sequence [49, 50]. The measured dephasing time T_2^{CPMG} for the V_2 (V_1/V_3) type of V_{Si}^- spin ensemble was 47 ± 7 μs (59 ± 3 μs) when the spacing between the refocusing pulses was 200 ns (100 ns), and the duration of each π pulse was 38 ns (40 ns). Details of the pulse sequence used and plots of the experimental data are given in appendix D.

Table 2, shows the comparison of the relaxation times measured in our previous paper where the 6H-SiC sample contained a higher concentration of ^{13}C but lower concentration of ^{29}Si [25]. In the present sample, T_1 is slightly longer than in the sample used in [25], which indicates a somewhat lower concentration of paramagnetic centers [44]. The longer dephasing times T_2^*, T_2 can be attributed to the lower concentration of ^{13}C, which represent the nearest neighbors (NN) of the silicon vacancy. The higher concentration of ^{29}Si does not have a significant effect, since the silicon atoms have a much weaker hyperfine interaction.

5. Discussion and conclusion

The V_{Si}^- center in SiC has attracted considerable interest in the context of emerging quantum technologies, since its spin can be optically polarized, has a sufficiently long coherence time and can be coherently controlled. These properties make it an attractive candidate for quantum information and quantum sensing. To develop this potential, it is essential to more precisely characterise its properties. They depend, e.g., on the lattice site at which the vacancy is created. In the 6*H*-SiC polytype, three different lattice sites exist, and the corresponding vacancies are referred to as V_1, V_2 and V_3.

In this work, we have gathered new data on all three types of vacancies. In particular, we related the properties of the PL of each center to the magnetic resonance by performing ODMR experiments for different directions of PL emission (parallel and perpendicular to the *c*-axis of the sample). V_1/V_3 emit preferentially in the direction of the *c*-axis while V2 emits preferentially perpendicular to *c*-axis. This observation supported the notion that the optical dipole orientation of V_2 differs from that of V_1 and V_3 [24]. ODMR experiments detecting photons that are emitted mostly by one type of center allowed us to determine the zero-field splitting of the V_1 vacancy, for which different values had been reported in previous works [14, 23]. Our results agree with those of [14]. With the identification of the ODMR frequencies of all three vacancies, we can explain the temperature dependence and change of sign of the ODMR signal near 28 MHz: At high temperature, the signal from V_3 dominates but at low temperature the signal from V_1 dominates, which is negative. In other defect systems such as NV in diamonds, the ZFS typically shows a small temperature variation. We checked the ZFS variation with temperature and found that the values increase by about 1 MHz as the temperature decreases from room temperature to 5 K. This variation is significantly smaller than the temperature variation of the excited state ZFS [36]. It is therefore possible to use the silicon vacancy for simultaneous measurements of the magnetic field and the temperature, using the ground state as magnetic field sensor and the excited state as temperature sensor [36].

We also measured the transverse and longitudinal relaxation rates. The relaxation rates measured here were lower than those reported earlier in a different sample [25] that contained a higher concentration of ^{13}C. Since ^{13}C is the next nearest neighbor to the vacancy, an increase in its concentration increases the rate of relaxation. However, reducing the concentration of ^{29}Si can compensate for this to some extent. Notably, the spin-echo decay for V_1/V_3, does not fit well to a single exponential, which is possibly due to the small difference in their ZFS and relaxation behavior. So, with the pulse measurements and temperature, we can separate the V_1 and V_3 ensemble signals. For example, the Rabi oscillations recorded at 5 K in Breev *et al* [24] were mainly due to V_1 vacancies, while at room temperature, they are mainly due to V_3 vacancies. The distinction between V_1 and V_3 vacancies could be ultimately clarified by repeating measurements on individual V_1 and V_3 vacancies. However, the background concentration of vacancies in the 6*H*-SiC samples currently available to us does not allow us to do so. In future work, we will try to obtain more specific data for the relaxation times of the different centers and determine the different hyperfine coupling constants, and utilize them for hyperpolarization applications [51–54].

Acknowledgments

Data availability statement

All data that support the findings of this study are included within the article (and any supplementary files).

Ethics statement

This article does not involve any research with human or animal participants conducted by the authors.

Note

All experiments were done on the sample provided by A N A and P G B well before the EU sanctions. H S and D S did experimental measurements and data analysis. To our knowledge, these results do not have any short-term economic or military relevance.

Conflict of interest

The authors declare no conflicts of interest.

Appendix A. Sample

SiC crystals were grown with a low content of background impurities from polycrystalline sources of semiconductor silicon and spectrally pure carbon. They were degassed using a resistive heating growth machine over 2 hours at 2200°C and 10^{-3} Torr to prepare the crucible and internal furnace reinforcement. After that, a stoichiometric mixture of carbon and silicon powders was loaded into the crucible. All components of the crucible were made from the same graphite (6516pT (Mersen, France)) to minimize stress due to from thermal expansion when the crucible is exposed to temperatures exceeding the synthesis temperature of the source (above 1600°C). We used silicon carbide crystals polytype 6*H* as seeds. To grow crystals, the following conditions were used: 2050 °C, 1 to 5 Torr argon pressure, 99.9999% pure argon, a growth rate of 150 μm / h. Crystals that grew under these conditions had less than 3 micropores per cm^2. The grown crystal was then cut into chips 2 inches (50 mm) in diameter and 300 μm thick. To create the V_{Si}^- centers, we performed electron irradiation with an energy of 2 MeV and a fluence of 10^{18} cm^{-2}, ensuring a homogeneous V_{Si}^- distribution and optimizing the ODMR signal-to-noise ratio [55].

Appendix B. PL setup

For measuring the photoluminescence (PL) at different temperatures, the sample was mounted on the cold finger of a helium flow cryostat (MicrostatHe-R from Oxford instruments) using silver glue. A tunable (799-813 nm) single-mode diode laser (DL pro from Toptica Photonics) was used to excite the sample optically. The laser beam was modulated by a chopper and focused onto the sample as shown in figure C1, using mirror M and lens L1, without an AOM in the laser path. Two convex lenses collected the PL, which was then filtered by an 850 nm long-pass filter (Thorlabs), and passed through a monochromator (Spex 1704). For detecting the PL, an avalanche photodiode (APD) module with a frequency bandwidth from dc to 100 kHz (C5460-1 series from Hamamatsu) was attached to the monochromator. The amplified photocurrent was measured with a lock-in amplifier (SRS model SR830 DSP) referenced to the sync signal of the chopper [25]. When recording the PL parallel to the crystal *c*-axis, the sample was positioned with the plane perpendicular to the *c*-axis towards the detector (as shown in the dashed rectangle instet labeled A1 in figure C1) . When recording PL perpendicular to the *c*-axis, the crystal was placed such that the *c*-axis formed a 90-degree angle with the detector (as shown in the dashed rectangle instet labeled A2 in figure C1). The laser beam was directed onto the surface facing the detector.

Appendix C. ODMR setup

Figure C1 shows the setup used for the cw- and time-resolved ODMR measurements. For cooling the sample, we used the helium flow cryostat. We used a turbopump (Pfeiffer) for creating a vacuum in the cryostat less than 10^{-6} mbar. A LD785-SE400 diode laser with a laser with a LDC202C series controller and a temperature controller (TED 200C) was used as the light source. Laser pulses were generated by an acoustic-optical modulator (NEC model OD8813A). We used three orthogonal coil pairs to apply a static magnetic field to the sample. An APD module with a frequency bandwidth from dc to 10 MHz (C12703 series from Hamamatsu) was used to collect the PL signal. For time-resolved experiments, the signal was digitized with a PicoScope 2000 USB oscilloscope card. For cw-ODMR, the signal from the APD was sent to the lock-in. An Analog Devices' AD9915 direct digital synthesizer (DDS) was used as an RF source for cw-ODMR experiments and a Hunter Micro DAx14000 arbitrary wave generator (AWG) for pulsed ODMR experiments. The RF signal from the source was amplified with an RF amplifier (LZY-22+ from Mini-Circuits). For feeding RF power to a sample, we used a wire (mounted directly over the sample labled S in figure C1) and a coil (as shown in dashed rectangle labeld A3 in figure C1), terminated with a 50-Ohm resistor for CW and pulsed ODMR experiments, respectively. We generated TTL pulses using a digital word generator (DWG; SpinCore PulseBlaster ESR-PRO PCI card) to trigger the laser and RF pulses.

C.1. Dependence on RF power
Figure C2 (a) shows ODMR spectra recorded with different RF powers at room temperature (296 K) and at 5 K. These spectra were recorded with an 850 nm long pass optical filter, which suppresses the scattered laser light but passes most of the PL from V_{si}^-. At low RF power, only two ODMR peaks are visible near 28 MHz and 130 MHz.
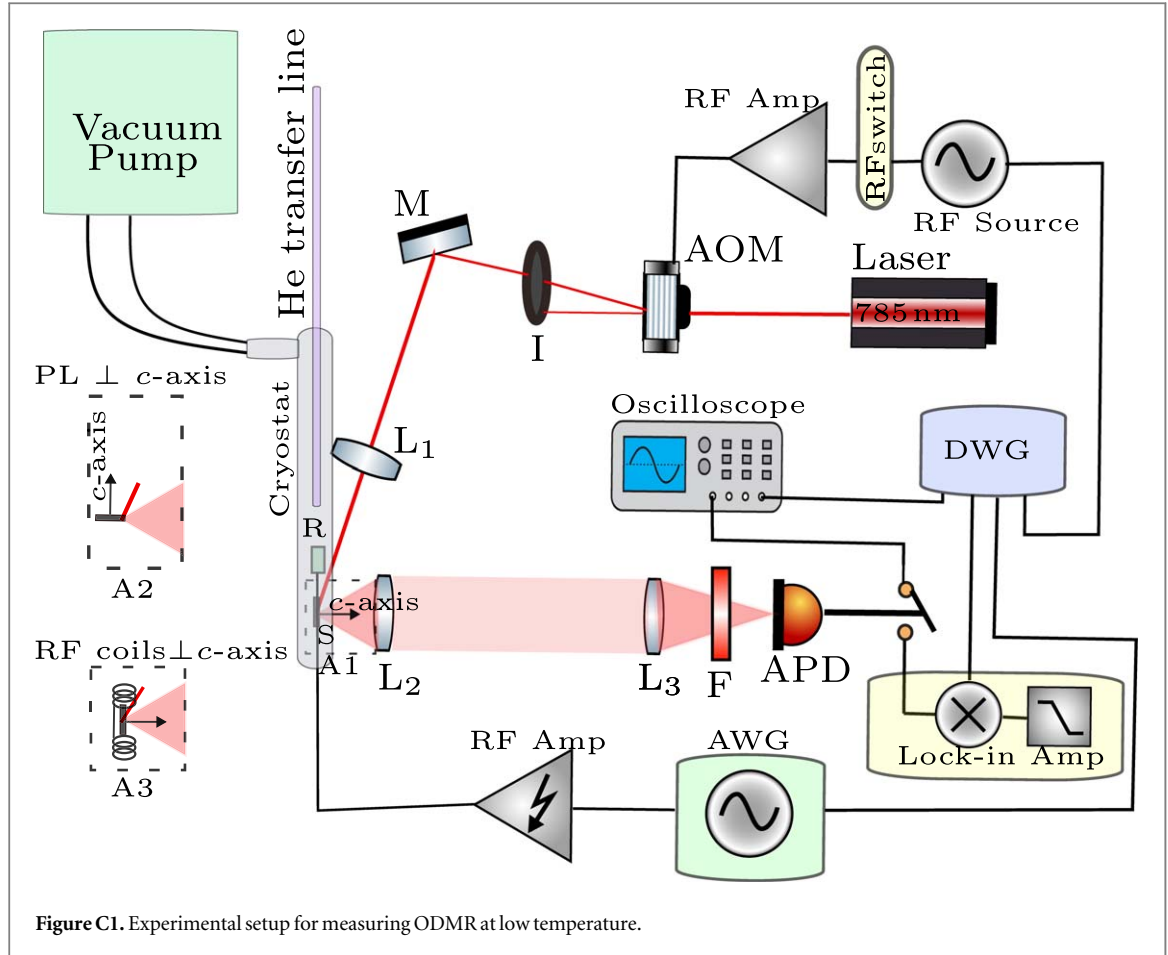
Figure C1. Experimental setup for measuring ODMR at low temperature.

Table C1. Fitting parameters of equations C1 and C2.

V_{si}^-	Temp	$S_{max}(\Delta PL/PL)$	$P_0(W)$	$LW_0(MHz)$	$a\,(MHz\,W^{-1/2})$
V_1/V_3	298 K	0.14 ± 0.01	0.05 ± 0.03	6.6 ± 0.4	3.4 ± 0.3
V_1/V_3	5 K	-0.014 ± 0.001	0.023 ± 0.012	5.5 ± 0.8	2.3 ± 0.7
V_2	298 K	-0.069 ± 0.007	0.070 ± 0.043	8.4 ± 0.7	3.7 ± 0.6
V_2	5 K	-0.234 ± 0.054	0.097 ± 0.097	7.5 ± 0.4	3.4 ± 0.4

With increasing RF power, additional resonances appear at 14 MHz (P_3^2), 42 MHz (P_2^3), and 64 MHz (P_2^2). The peak P_3^2 is due to the absorption of 2 RF photons by the V_1/V_3 vacancy [28], whereas the peaks P_2^2 and P_2^3 are due to 2 and 3 photon absorption by the V_2 vacancy [28]. Some shoulders are not labeled, which could potentially be attributed to the hyperfine coupling between V_{Si}^- and the nuclear spins, primarily ^{29}Si, given its higher concentration in this sample. For instance, the peaks at 43 and 25 MHz are likely due to the splitting induced by ^{29}Si in the V_1/V_3 vacancy levels [56]. However, a detailed analysis of these effects is beyond the scope of this paper. Figure C2 (b) shows the amplitudes of the 1-photon peaks of V_1/V_3 and V_2 versus the applied RF power: they increase with the applied power but saturate for $P > 0.3$ W. This behaviour can be fitted with the function
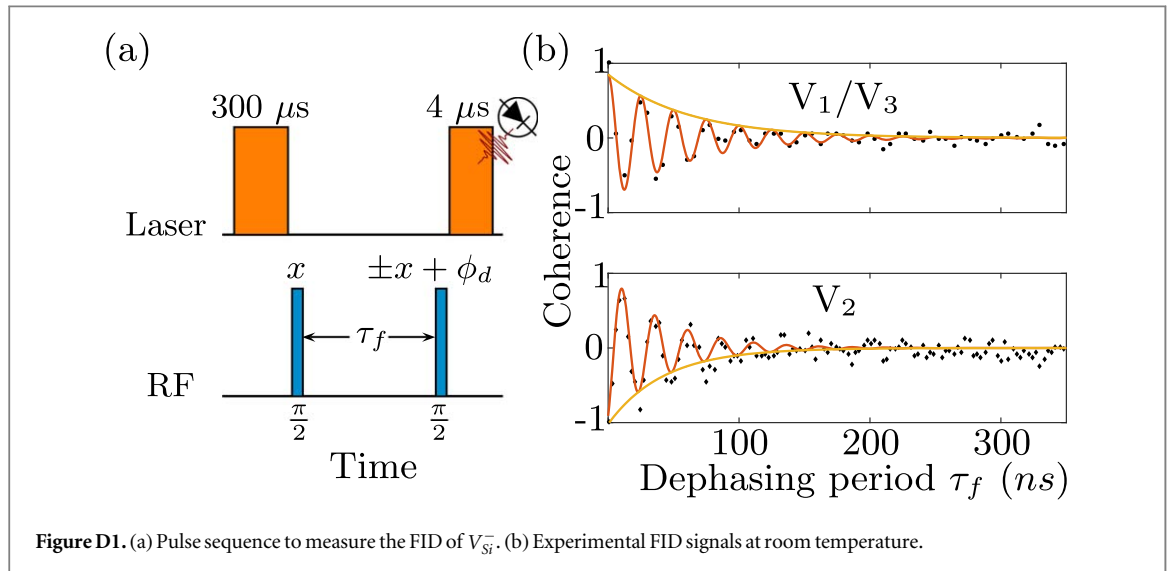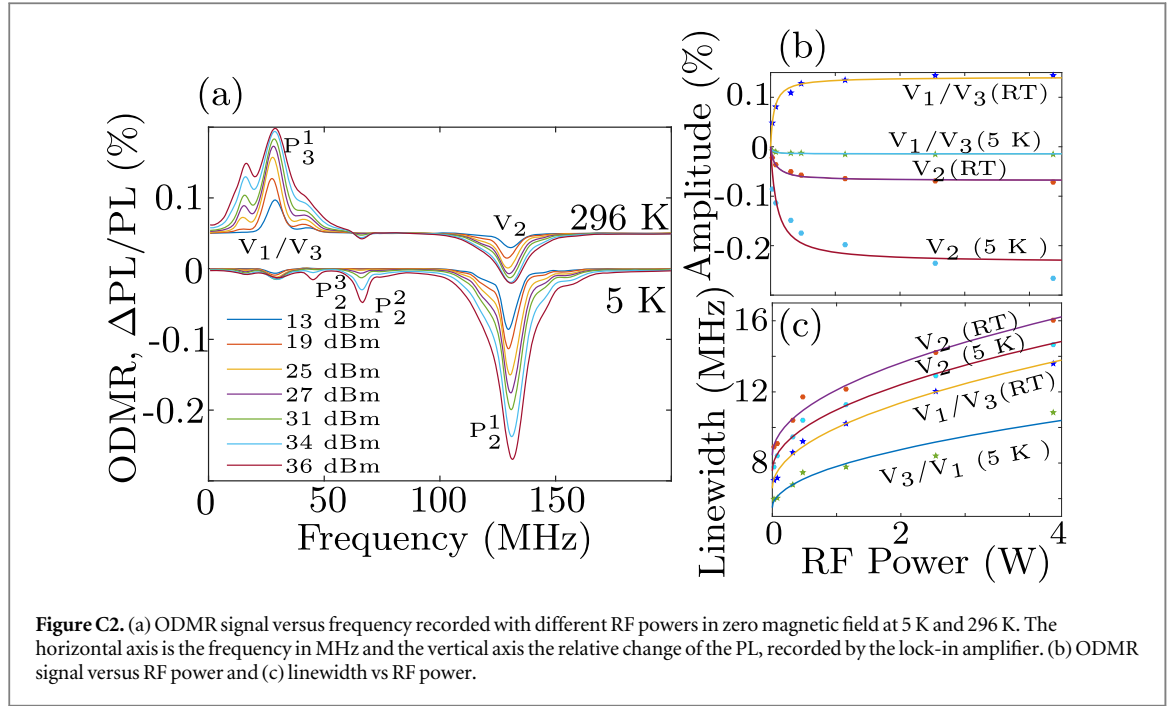
$$S(P) = S_{max}[P/(P_0 + P)], \tag{C1}$$

where $S(P)$ is the signal amplitude at power P, S_{max} is the asymptotic amplitude and P_0 the saturation power. The resulting fitting parameters are given in table C1.

Figure C2 (c) shows the linewidths of the 1-photon peaks of V_1/V_3 and V_2 versus the RF power. The linewidth data $LW(P)$ were fitted to the function

$$LW(P) = LW_0 + a\sqrt{P}, \tag{C2}$$

where LW_0 and a are fitting parameters and the fitted values are given in table C1. At room temperature, the fitting parameter LW_0 for the sample with inverted isotope concentration [25] was 6.2 MHz (7.9 MHz) for $V_1/V_3(V_2)$, respectively.

Figure C2. (a) ODMR signal versus frequency recorded with different RF powers in zero magnetic field at 5 K and 296 K. The horizontal axis is the frequency in MHz and the vertical axis the relative change of the PL, recorded by the lock-in amplifier. (b) ODMR signal versus RF power and (c) linewidth vs RF power.

Figure D1. (a) Pulse sequence to measure the FID of V_{Si}^-. (b) Experimental FID signals at room temperature.

Appendix D. FID and CPMG

Figure D1(a) shows the pulse sequence for the FID measurement. A laser pulse of 300 μs and a power of 100 mW was used to polarize the vacancy spin ensemble. A delay τ_f was given between the two $\pi/2$ RF pulses, and the PL signal was obtained using the second laser pulse. The phase of the first $\pi/2$ pulse was along x. For the second $\pi/2$ pulse, it was along x$+\phi_d$. We repeated the same sequence for the reference scan except for the phase of the second $\pi/2$ pulse was $-x + \phi_d$. Here the $\phi_d = \nu_{det}\tau_f$ and the detuning frequency was $\nu_{det} = 40$ MHz. Figure D1(b) shows the signals recorded for both V_{Si}^- as a function of the dephasing delay τ_f. The experimental signal of V_2 (V_3) was fitted to the function

$$S_{x+\phi_d} - S_{-x+\phi_d} = A \cos(2\pi\nu_{det}\tau_f + c)e^{-\tau_f/T_2^*}, \tag{D1}$$

where $S_{\pm x+\phi_d}$ is the average PL signal measured with a $\pi/2$ RF detection pulse of phase $\pm x + \phi_d$. Fitting the experimental signal using equation (D1) led to $T_2^* = 42$ ns (65 $\pm$ 5 ns).

Figure D2(a) shows the pulse sequence for measuring the spin coherence time under the CPMG sequence. We first polarized the spin ensemble with the 300 μs laser pulse and created the coherence with the first $\pi/2$ pulse. The CPMG sequence was applied i.e., a train of $2N \pi$ pulses applied along the y-axis, which were separated

Figure D2. (a) Pulse sequence for measuring the spin coherence time under the CPMG sequence. (b) Experimental decay of the spin coherence during the CPMG sequence at room temperature.
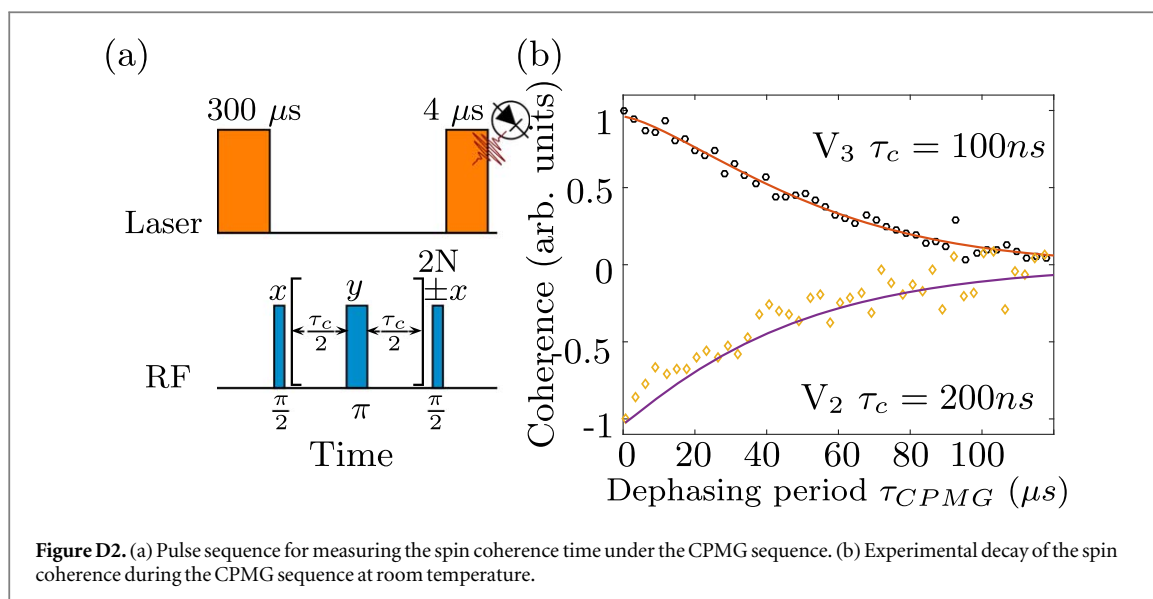
by a delay of $\tau_c/2$ from each other. Finally, the coherence was coverted into a population by the second $\pi/2$ pulse along the x-axis and the PL signal was measured with the second laser pulse. A reference signal was recorded with the same pulse sequence, but the second $\pi/2$ pulse was applied along the $-x$-axis. The difference between the experimentally measured PL signals was fitted to the function.

$$S_x - S_{-x} = A\ e^{-(\tau_{CPMG}/T_2^{CPMG})^n},\tag{D2}$$

where the total duration is $\tau_{CMPG} = 2N(\tau_c + \tau_{\pi pulse})$ 2N is number of π pulses and $\tau_{\pi pulse}$ is the duration of a π pulse, which was 20 ns for V_1/V_3 and V_2.

ORCID iDs

Harpreet Singh ⬤ https://orcid.org/0000-0002-7505-4850
Andrey N Anisimov ⬤ https://orcid.org/000-0003-2171-7943
Pavel G Baranov ⬤ https://orcid.org/000-0003-1955-9245
Dieter Suter ⬤ https://orcid.org/0000-0002-7349-3032

References

[1] Wang J, Zhou Y, Zhang X, Liu F, Li Y, Li K, Liu Z, Wang G and Gao W 2017 *Phys. Rev. Applied* **7** 064021
[2] Rabkowski J, Peftitsis D and Nee H 2012 *IEEE Ind. Electron. Mag.* **6** 17–26
[3] Izhevskyi V, Genova L, Bressiani J and Bressiani A 2000 *Structure, Properties and Processing Cerâmica* **46** 4–13
[4] Gonzalez Szwacki N 2017 *Computational Condensed Matter* **13** 55–8
[5] Pavunny S P, Yeats A L, Banks H B, Bielejec E, Myers-Ward R L, DeJarld M T, Bracker A S, Gaskill D K and Carter S G 2021 *Sci. Rep.* **11** 3561
[6] Vasquez G C *et al* 2020 *Nano Lett.* **20** 8689–95
[7] Babin C *et al* 2022 *Nat. Mater.* **21** 67–73
[8] Morioka N *et al* 2020 *Nat. Commun.* **11** 2516
[9] Sörman E, Son N T, Chen W M, Kordina O, Hallin C and Janzén E 2000 *Phys. Rev. B* **61** 2613–20
[10] Widmann M *et al* 2015 *Nat. Mater.* **14** 164–8
[11] Csóré A, Son N T and Gali A 2021 *Phys. Rev. B* **104** 035207
[12] Nagy R *et al* 2019 *Nat. Commun.* **10** 1954
[13] Wang J F *et al* 2019 *ACS Photonics* **6** 1736–43
[14] Davidsson J, Ivády V, Armiento R, Ohshima T, Son N T, Gali A and Abrikosov I A 2019 *Appl. Phys. Lett.* **114** 112107
[15] Liu L *et al* 2022 *Nano Lett.* **22** 9943–50
[16] Lin W X *et al* 2021 *Phys. Rev. B* **104** 125305
[17] Castelletto S and Boretti A 2020 *Journal of Physics: Photonics* **2** 022001
[18] Castelletto S, Peruzzo A, Bonato C, Johnson B C, Radulaski M, Ou H, Kaiser F and Wrachtrup J 2022 *ACS Photonics* **9** 1434–57
[19] Riedel D, Fuchs F, Kraus H, Väth S, Sperlich A, Dyakonov V, Soltamova A A, Baranov P G, Ilyin V A and Astakhov G V 2012 *Phys. Rev. Lett.* **109** 226402
[20] Wagner M, Magnusson B, Chen W M, Janzén E, Sörman E, Hallin C and Lindström J L 2000 *Phys. Rev. B* **62** 16555–60
[21] Baranov P G, Bundakova A P, Soltamova A A, Orlinskii S B, Borovykh I V, Zondervan R, Verberk R and Schmidt J 2011 *Phys. Rev. B* **83** 125203
[22] Ivády V, Davidsson J, Son N T, Ohshima T, Abrikosov I A and Gali A 2017 *Phys. Rev. B* **96** 161114
[23] Biktagirov T, Schmidt W G, Gerstmann U, Yavkin B, Orlinskii S, Baranov P, Dyakonov V and Soltamov V 2018 *Phys. Rev. B* **98** 195204

[24] Breev I *et al* 2022 *npj Quantum Information* **8** 1–9

[25] Singh H, Anisimov A N, Nagalyuk S S, Mokhov E N, Baranov P G and Suter D 2020 *Phys. Rev.* B **101** 134110

[26] Fuchs F, Stender B, Trupke M, Simin D, Pflaum J, Dyakonov V and Astakhov G 2015 *Nat. Commun.* **6** 1–7

[27] Kasper C A 2021 Engineering of highly coherent silicon vacancy defects in silicon carbide *Ph.D. Thesis* Universität Würzburg

[28] Singh H, Hollberg M A, Anisimov A N, Baranov P G and Suter D 2022 *Phys. Rev. Research* **4** 023022

[29] Zhou J Y *et al* 2021 *ACS Photonics* **8** 2384–91

[30] Janzén E, Gali A, Carlsson P, Gällström A, Magnusson B and Son N T 2009 *Physica B* **404** 4354–8

[31] Singh H, Anisimov A N, Breev I D, Baranov P G and Suter D 2021 *Phys. Rev.* B **103** 104103

[32] Carbonera D 2009 *Photosynth. Res.* **102** 403

[33] Davies J 1976 *Contemp. Phys.* **17** 275–94

[34] Lifshitz E, Fradkin L, Glozman A and Langof L 2004 *Annu. Rev. Phys. Chem.* **55** 509–57

[35] Astakhov G, Simin D, Dyakonov V, Yavkin B, Orlinskii S, Proskuryakov I, Anisimov A, Soltamov V and Baranov P 2016 *Appl. Magn. Reson.* **47** 793–812

[36] Anisimov A, Simin D, Soltamov V A, Lebedev S P, Baranov P G, Astakhov G V and Dyakonov V 2016 *Sci. Rep.* **6** 33301

[37] Udvarhelyi P 2020 *Phys. Rev. Appl.* **13** 054017

[38] Ivády V, Simon T, Maze J R, Abrikosov I A and Gali A 2014 *Phys. Rev.* B **90** 235205

[39] Breev I D, Poshakinskiy A V, Yakovleva V V, Nagalyuk S S, Mokhov E N, Hübner R, Astakhov G V, Baranov P G and Anisimov A N 2021 *Appl. Phys. Lett.* **118** 084003

[40] Abragam A 1961 *The Principles of Nuclear Magnetism* (Oxford University Press)

[41] Slichter C P 2013 *Principles of Magnetic Resonance* (Berlin, Heidelberg: Springer Science & Business Media) 3 vol 1 (https://doi.org/10.1007/978-3-662-09441-9)

[42] Mehring M 2012 *High Resolution NMR Spectroscopy in Solids* (Berlin, Heidelberg: Springer Science & Business Media) vol 11 (https://doi.org/10.1007/978-3-642-96332-2)

[43] Carter S G, Soykal O O, Dev P, Economou S E and Glaser E R 2015 *Phys. Rev.* B **92** 161202(R)

[44] Simin D, Kraus H, Sperlich A, Ohshima T, Astakhov G V and Dyakonov V 2017 *Phys. Rev.* B **95** 161201

[45] Bulancea-Lindvall O, Son N T, Abrikosov I A and Ivády V 2021 *NPJ Comput. Mater.* **7** 213

[46] Levitt M H 2013 *Spin dynamics: basics of nuclear magnetic resonance* (Wiley)

[47] Ramsey N F 1950 *Phys. Rev.* **78** 695–9

[48] Hahn E L 1950 *Phys. Rev.* **80** 580–94

[49] Meiboom S and Gill D 2004 *Rev. Sci. Instrum.* **29** 688–91

[50] Carr H Y and Purcell E M 1954 *Phys. Rev.* **94** 630

[51] Sahin O, de Leon Sanchez E, Conti S, Akkiraju A, Reshetikhin P, Druga E, Aggarwal A, Gilbert B, Bhave S and Ajoy A 2022 *Nat. Commun.* **13** 5486

[52] Beatrez W, Pillai A, Janes O, Suter D and Ajoy A 2023 *Phys. Rev. Lett.* **131** 010802

[53] Lv X *et al* 2021 *Proc. Natl Acad. Sci.* **118** e2023579118

[54] Bucher D B, Glenn D R, Park H, Lukin M D and Walsworth R L 2020 *Phys. Rev. X* **10** 021053

[55] Kasper C *et al* 2020 *Phys. Rev. Appl.* **13** 044054

[56] Soltamov V A, Yavkin B V, Mamin G V, Orlinskii S B, Breev I D, Bundakova A P, Babunts R A, Anisimov A N and Baranov P G 2021 *Phys. Rev.* B **104** 125205

PAPER · OPEN ACCESS

Zero-Field ODMR and relaxation of Si-vacancy centers in 6H-SiC

To cite this article: Harpreet Singh *et al* 2023 *Mater. Res. Express* **10** 116201

View the article online for updates and enhancements.

You may also like